Nanoscale

PAPER

Cite this: *Nanoscale*, 2021, **13**, 3841

An integrated and multi-technique approach to characterize airborne graphene flakes in the workplace during production phases

Francesca Tombolini, *[a] Fabio Boccuni,[a] Riccardo Ferrante,[a] Claudio Natale,[a,b] Luigi Marasco,[c] Elisa Mantero,[c,f] Antonio Esau Del Rio Castillo, [c,f] Luca Leoncino,[d] Vittorio Pellegrini,[c,f] Stefania Sabella [e] and Sergio Iavicoli[a]

Graphene is a one-atom-thick sheet of carbon atoms arranged in a honeycomb pattern and its unique and amazing properties make it suitable for a wide range of applications ranging from electronic devices to food packaging. However, the biocompatibility of graphene is dependent on the complex interplay of its several physical and chemical properties. The main aim of the present study is to highlight the importance of integrating different characterization techniques to describe the potential release of airborne graphene flakes in a graphene processing and production research laboratory. Specifically, the production and processing (*i.e.*, drying) of few-layer graphene (FLG) through liquid-phase exfoliation of graphite are analysed by integrated characterization techniques. For this purpose, the exposure measurement strategy was based on the multi-metric tiered approach proposed by the Organization for Economic Cooperation and Development (OECD) *via* integrating high-frequency real-time measurements and personal sampling. Particle number concentration, average diameter and lung deposition surface area time series acquired in the worker's personal breathing zone (PBZ) were compared simultaneously to background measurements, showing the potential release of FLG. Then, electron microscopy techniques and Raman spectroscopy were applied to characterize particles collected by personal inertial impactors to investigate the morphology, chemical composition and crystal structure of rare airborne graphene flakes. The gathered information provides a valuable basis for improving risk management strategies in research and industrial laboratories.

Received 5th October 2020,
Accepted 19th January 2021

DOI: 10.1039/d0nr07114e

rsc.li/nanoscale

Introduction

The rapid growth of nanotechnology together with the production of engineered nanomaterials and their consequent wide diffusion and distribution at the global scale, has inevitably increased the likelihood of exposure for workers employed in the production, handling and use of nanomaterials.[1]

Despite the increasing production and use of nanomaterials with their possible impact on human health, there are few studies on the safety levels of exposure to nanomaterials, in the workplace or in daily life environments.[2]

One of the nanomaterials with potential use in daily life environments is graphene. Graphene is a two-dimensional (2D) crystal consisting of a single atomic layer of sp^2-hybridised carbon atoms arranged in a honeycomb lattice, first isolated in 2004.[3] Its unique electrical, thermal, optical and mechanical properties allow graphene to act as a suitable platform for different applications in nanoelectronics, transparent conducting electrodes, energy storage, and sensors.[4]

Graphene can be synthesized using various physical and chemical methods.[5,6] Different methods of synthesis can give rise to different morphologies such as sheets,[7] platelets,[8] ribbons[9] or quantum dots.[10] Several studies on the toxicity of graphene report that it depends on several physical–chemical properties, *e.g.*, morphology, size, carbon–oxygen ratio, type and quantity of functional groups, and dispersion state. Additionally, the route and dose of administration and the exposure times are of paramount importance in assessing the toxicity.[11,12] The use of standardized and validated characteriz-

[a]*Italian Workers' Compensation Authority—Department of Occupational and Environmental Medicine, Epidemiology and Hygiene, Via Fontana Candida 1, I-00078 Rome, Italy. E-mail: f.tombolini@inail.it*
[b]*Sapienza University of Rome, Nanotechnology Research Center Applied to Engineering (CNIS) Rome, Italy*
[c]*Istituto Italiano di Tecnologia, Graphene Labs, Via Morego, 30-16136 Genoa, Italy*
[d]*Istituto Italiano di Tecnologia, Drug Discovery and Development Department, Via Morego, 30-16136 Genoa, Italy*
[e]*Istituto Italiano di Tecnologia, Electron Microscopy Facility, Via Morego, 30-16136 Genoa, Italy*
[f]*BeDimensional S.p.a, Via Lungotorrente Secca, 3d-16163 Genoa*

ation techniques for the toxicology evaluation of graphene-like materials plays a key role when the properties of the material are connected to its biological effects.[13,14]

In particular, workers involved in the research and development (R&D) of graphene and other nanocrystals are among the first people who could be exposed to breathable graphene powder.[15] Specifically, graphene powder can be released in the workplace environment during the production or processing phases, *e.g.* reactor cleaning and powder handling and storage,[16] with the consequent risk of being inhaled and settling in workers respiratory tract. Additionally, dermal exposure to graphene may also occur.[17] Different exposure measurement strategies in occupational environments deal with common problems, such as natural and anthropogenic nanoparticles in workplace air and the use of different metrics to characterize parameters can induce adverse effects on human health.[8,18,19]

In particular, the concentration of nanomaterials in the workplace environment can be described using metrics such as mass per volume or number of particles per volume.[20] Very limited data are currently available on airborne graphene-based material concentrations in occupational settings.[14] At present, no official occupational exposure limits (OELs) for graphene are available.[21] Lee *et al.*[22] proposed an OEL of 18 μg m^{-3} for graphene from subchronic inhalation study data in rats.

Properties of nano-objects, such as their surface and particle number concentration (PNC), are considered to be better metrics of exposure than mass concentration.[20] The number concentration corresponding to a mass concentration of 0.1 mg m^{-3} was calculated for several engineered nanomaterials and the nano reference value (NRV) is considered to be 40 000 particles per cm^3 for particles with densities lower than 6 g cm^{-3}.[20]

Furthermore, the measurement of lung deposited surface area (LDSA), taking into account the deposition efficiency of airborne objects in different compartments of the lung, is considered a relevant metric to investigate the negative health effects of aerosol nanoparticles. Toxicological studies report that LDSA correlates with negative health effects.[23,24]

In this study, the exposure measurement and sampling strategy is based on the guidelines published by the Organization for Economic Cooperation and Development (OECD), reporting a harmonized multi-metric tiered approach.[25,26]

Tier 1 is focused on gathering information about the workplace activity and the physical and chemical properties of the engineered nanomaterials and exposure scenario.

Tier 2 consists of *in situ* investigations to conduct basic exposure assessment using easy to use and portable equipment to measure airborne nanomaterials by real time measurements and sampling for further off-line analysis. Electron microscopes are among the instruments most commonly used at this tier to investigate the nanomaterials' morphology and elemental composition by energy dispersive X-ray spectroscopy (EDS).

Tier 3 includes an expert exposure assessment using all appropriate equipment and available characterisation techniques (*e.g.*, Raman spectroscopy, inductively coupled plasma-mass spectroscopy, gas chromatography–mass spectroscopy, asymmetric flow field flow fractionation, infrared spectroscopy) to provide a definitive conclusion regarding the presence of airborne nanomaterials in the occupational setting.

The multi-metric approach provides for an evaluation of the results at the end of each investigation tier, based on specific decision criteria and compares the exposure parameters with their corresponding background values.[25,26]

A comprehensive evaluation of worker exposure to few-layer graphene (FLG),[27] based on the OECD approach and integrated with biological monitoring,[28] has recently been proposed, showing that the presence of airborne FLG in the workplace atmosphere should not be excluded, but must be carefully investigated, and it is indispensable to integrate electron microscopy techniques and Raman spectroscopy to examine the presence of FLG in the work environment.

In this framework, the goal of this study is to determine the presence of FLG released during its production and handling in a research laboratory. Specifically, the production of FLG is performed by liquid phase exfoliation (LPE), obtaining a dispersion of flakes in an organic solvent. The source of airborne graphene flakes is mainly due to the powder obtained by the freeze-drying of the FLG dispersion. According to the OECD methodology, high resolution real-time measurements of PNC, average diameter and LDSA are performed during specific production phases and compared to the background.

Scanning and transmission electron microscopies (SEM and TEM) and Raman spectroscopy are used to characterize the morphology, chemical composition and crystal structure of the airborne particles. The particles are collected by inertial impactors (see Material and methods section for further details) in the workers' personal breathing zone (PBZ).

Materials and methods

Few layer graphene production phases

Few layer graphene (FLG) production encompasses four phases.

- The exfoliation phase is performed by the wet-jet-milling (**WJM phase**) technique.[6] Briefly, a mixture of graphite crystals (Sigma Aldrich, 150 mesh) is dispersed in *N*-methyl-2-pyrrolidone (NMP) at a concentration of 10 g L^{-1} and processed through the WJM (Jokho, Japan WJM100), *i.e.*, the dispersion is forced to pass through narrow nozzles with diameters of 300, 200, 150 and 100 μm using pressures increasing from 150 to 250 MPa. The exfoliation process for 10 L takes 8 hours in the WJM.

- In the solvent exchange, the NMP is removed *via* rotary evaporation (**RV phase**) (Heidolph, Hei-Vap Value, 70 °C, 5 mbar). At this stage, the product is a paste-like material. Dimethyl sulphoxide is added to obtain a FLG concentration of 30 g L^{-1}. The time averaged duration is 8 hours.

- In the **LIO phase**, the graphene powder is finally obtained *via* freeze drying. The dispersion is consequently poured into aluminium Petri dishes (300 ml capacity) and placed in a refrigerator at −15 °C. After ∼1 h, the petri dishes are put inside a single-chamber freeze dryer (Martin Christ Alpha 2-4LSC plus), where the temperature the condenser is already set to −85 °C. The sublimation is carried out at a temperature of −10 °C and a pressure of 0.1 mbar. After 50 hours, the final powder is extracted from the freeze dryer.

- For storage and cleaning (**STOCLE phase**), after the LIO phase, the freeze dryers are opened and the Petri dishes (freeze dryer containers) are stored under a recirculation hood (Erlab Captair 483 Smart). The time averaged duration is 3 hours for this phase.

The crystals obtained *via* WJM were intensely characterised by TEM, AFM, SEM, and Raman and X-ray photoelectron spectroscopies.[6,11,29,30]

Table 1 summarizes the physical and chemical properties of the FLG and the laboratory structure and characteristics (ventilation type and safety features).

Real time measurements

Particle number concentration values (PNC, particles per cm^3) were obtained using a condensation particle counter (CPC model 3007, TSI Inc., Shoreview, MN, USA) that measures airborne particles from 10 nm to 1 μm, with a time resolution of 1 s and an accuracy of ±20% (total flow 0.7 L min^{-1}, detection limits 1 to 100 000 particles per cm^3).

Two mini diffusion size classifiers (DISCmini, TESTO) were used to measure the PNCs (particles per cm^3) in the range of 10–700 nm and both the average diameter (nm) and the LDSA (μm^2 cm^{-3}) in the range of 10–300 nm, with a time resolution of 1 s and accuracy of ±30% (total flow 0.99 L min^{-1}, detection limits 1 to 100 000 particles per cm^3).

The CPC and DISCmini (DM) operational modes are described in detail in the ref. 31.

Microclimatic probes integrated in a control unit (BABUC-A, Lsi-Lastem Inc., Milano, Italy) were also used to measure the temperature and relative humidity (RH) in real time.

The CPC and the two DMs (DM-UF3 and DM-UF5) operate in different particle diameter ranges. To get reliable measurements, simultaneous samplings are performed by positioning the air-sampling probes close to each other to verify their linear correlation when testing in the same environmental conditions. The CPC was chosen as a reference for the PNC, having lower accuracy than the DMs.[27,32]

The slope (m) and the intercept (b) values obtained from the linear correlation between PNCs acquired by CPC and DM-UF3 are $m_{\text{CPC-UF3}} = 1.4$ and $b_{\text{CPC-UF3}} = -102.5$ particles per cm^3 ($R^2 = 0.95$) and those for CPC and DM-UF5 are $m_{\text{CPC-UF5}} = 1.1$ and $b_{\text{CPC-UF5}} = 385.6$ particles per cm^3 ($R^2 = 0.98$). These coefficients are also used to align the PNC values of area measurements, regardless of whether they were acquired by the CPC or by the DMs.[33]

Integration time sampling and off-line measurements

The inertial cascade impactor is a time-integrated instrument that selects, collects and fractionates particles of various sizes on different supports, *e.g.*, metal foils, plastic films or filter media.[31]

In this study, a personal sampling impactor (Sioutas, SKC Inc., Eighty Four, PA, USA) equipped with a pump (Tecora, 9 L min^{-1} flow) was used. Aluminium filters were used to collect airborne particles with aerodynamic diameters greater than 2500 nm (stage A), from 2500 to 1500 nm (stage B), 1500 nm to 500 nm (stage C) and 500 nm to 250 nm (stage D). A further fraction smaller than 250 nm was collected on a polycarbonate filter. Two different kinds of samples were considered. The first is the FLG powder sample, the '**trial sample**' obtained at the end of the production phases; the second, the '**Sioutas**

Table 1 General information for the powder-like material and laboratory

Powder technical name	Few layer graphene (FLG)
Physical state	Solid, powder form (black)
Surface chemistry	Nitrogen and oxygen traces (solvent residual)
Production method	Wet jet mill (high pressure homogeniser)
Aggregation/agglomeration	Possible aggregation due to electrostatic attraction among the flakes
Solubility	Insoluble in water
Dispersibility	Dispersible in NMP, DMSO, tetrahydrofuran, cyclohexyl pyrrolidone, *etc.*
Dustiness (or bulk material density)	Average bulk densities Untapped: 0.034185 g cm^{-3} Tapped: 0.046785 g cm^{-3}
Size	Lateral size mode in the range 100–1000 nm Thickness between 1 to 5 nm
Average quantity produced/used per month	500 g
Average quantity produced/used in each process	Max 100 g
Laboratory ventilation system	Mechanical ventilation system producing an air change of 3 volumes per hour
Protective equipment	Collective protective equipment: recirculating hood (Erlab Captair 483 Smart), aspiration arms Personal protective equipment: suits, coats, nitrile gloves, cold resistant gloves, arm sleeves, glasses, masks ABEK1P3RD (3 M 4279), ear protection headphones (3 M Peltor ProTac III e mod. X3A)

samples', are the samples collected on the Sioutas filters during the production phases.

The trial sample was dispersed in 2-propanol and sonicated for 15 minutes. The suspension was drop-cast on a stub covered with an aluminium filter.

The aluminium and polycarbonate Sioutas filters are directly mounted on stubs. The polycarbonate filter is then sputtered with Au while the Al filters are used with no post-treatment. Both samples are analysed by electron microscopes (SEM and TEM) and spectroscopy techniques (energy dispersive spectroscopy (EDS) and Raman).

The field emission scanning electron microscope (FegSEM, Zeiss) is equipped with an energy dispersive X-ray spectroscopy unit (EDS, Oxford Instruments INCA); the acquisition parameters are EHT = 2KV, working distance 5 mm, and a secondary electron signal.

The scanning electron microscope (SEM, JEOL JSM-6490LA) works with a thermoionic source (W filament) and is equipped with an energy dispersive X-ray spectroscope.

A micro Raman spectrometer (Renishaw, InVia) coupled to an excitation wavelength of 514 nm (power of 4 mW and 5 s of excitation time) was used for the Raman characterisation. The Raman mapping areas were constructed using Wire software, covering areas from 500 × 500 to 1000 × 1000 μm^2. The mappings were performed using a fixed Raman shift from 800 to 2200 cm^{-1}. The spectra were normalized and noise-filtered. The aluminium and polycarbonate filter stages were attached to glass substrates with adhesive tape.

A JEM-1400Plus TEM, with a thermionic source (LaB_6), operated at 120 kV, was used to acquire bright field TEM (BF-TEM) images and selected area electron diffraction (SAED) patterns. The central area of the Sioutas Al filter was immersed in ethanol (100 μL) and sonicated for 15 minutes at maximum power. The suspension was transferred onto the TEM grid (ultrathin carbon film on lacey carbon film, 400 mesh Cu) by drop-casting a 10 μL-droplet.

Airborne graphene monitoring

In the workplace, real-time instruments were positioned within 1.5 m of the workstations for area measurements. Furthermore, the workers wore personal samplers (personal measurements) with the sampling probes placed in the worker's breathing zone (PBZ), as shown in Fig. 1.

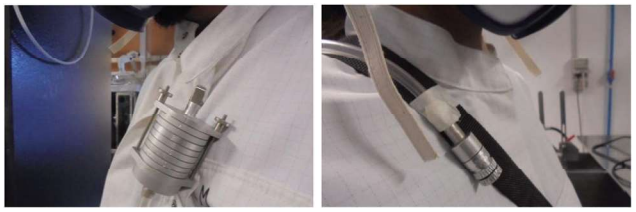

Fig. 1 Sioutas personal inertial cascade impactor worn by a worker (left side). DM sampling probe placed in the worker's breathing zone (right side).

The WJM and STOCLE phases were monitored in a single production day. The WJM phase took place in the morning from 10:49 to 12:22, producing about two litres of graphene ink. The STOCLE phase took place in the afternoon, from 15:11 pm to 17:48 pm, during which ten petri dishes from the two freeze dryers that had already completed the 50 h cycle (stored days before) were unloaded and stored. The RV and LIO phases were not monitored during the present study.

Results and discussion

Real time measurements

To investigate the potential release of graphene in powder form during the exfoliation and manipulation processes, *i.e.*, in the WJM and STOCLE phases, the characterization parameters of the background were used as control samples. Background parameters can be measured in (1) a workplace with the same structure where no nanomaterials are produced (the so-called background far field (FF)) or (2) in the same nanomaterial production site, but in non-productive periods (known as the background near field (NF)).[34]

In the present study, the FF background was chosen to be the laboratory contiguous to the graphene synthesis laboratory, as both share the same structural characteristics and forced ventilation; FF background measurements were performed simultaneously with those in the graphene laboratory during FLG production phases. Any differences in the measured parameters can be traced back to specific events related to the production phases performed inside the graphene laboratory.

Fig. 2a shows the PNC boxplots obtained from the CPC and DMs and used for area measurements during the WJM and the STOCLE phases to compare them with the corresponding FF backgrounds (WJM_{FF} and $STOCLE_{FF}$, respectively). The minimum and maximum values are indicated by the whiskers; median and mean values are indicated by the square and the line in the box, respectively.

The mean values of PNC in the boxplots (interquartile distance values in parenthesis) show a decrease from the morning, during the WJM phase (5109 (920) particles per cm^3), to the evening, during the STOCLE phase (3078 (1372) particles per cm^3). The same behaviour follows for the background WJM_{FF} (5583 (926) particles per cm^3) and the $STOCLE_{FF}$ (4484 (2471) particles per cm^3). In this case, the decreasing PNC could be due to environmental conditions. During the WJM phase, the forced ventilation system (which is the same for both the laboratory and the background FF) and the suction hoods were turned on. For the STOCLE phase, the forced ventilation was interrupted and only the suction hoods were operational; therefore, in the laboratory, the PNC values are lower than the background FF. Additionally, differences due to the forced ventilation system during the WJM and STOCLE phases were detected using microclimate probes, which measured constant values for the ambient temperature (T ambient 19.5 °C) and RH (62%) during the WJM phase and a temperature increase of about 3 °C and a RH drop of about

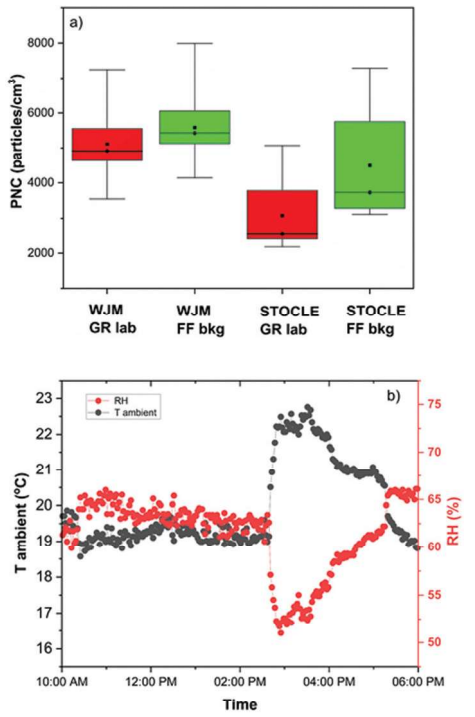

Fig. 2 Particle number concentration plots during (a) the WJM and STOCLE phases measured in the graphene laboratory (red boxplots) and in the background FF (green boxplots). (b) Time series of ambient temperature (black curve) and relative humidity (red curve).

15% during the STOCLE phase (Fig. 2b). Moreover, the STOCLE interquartile distance of PNC in the background FF can be explained due to the fact that the FF background is a passage to an external corridor and, therefore, the environment and the measurements could be influenced by air movements generated when people walk or when doors open and close.

According to the exposure characterization strategy, the next step is the analysis of the high-resolution time series of the PNC, average diameter and LDSA signals. This last gives information about the active particle area concentration in the lung alveolar compartment, taking into account the deposition efficiency of particles based on the model published by the International Commission on Radiological Protection.[35,36]

In the graphene laboratory, the measurements are carried out using DM for personal sampling (in contrast, the DM was used as area sampling in the background FF).

The time series of PNC (black curve) and average diameter (red curve) during the WJM and STOCLE phases are respectively reported in Fig. 3 and 4. A statistically significant value for PNC is defined as the average PNC calculated during the background NF plus three times the corresponding standard deviation;[37] all the PNC values greater than the significant value can be attributed to nanomaterial production and, in the case of the graphene laboratory, the significant value is 7376 particles per cm^3.

During the WJM phase (Fig. 3), the PNC time series acquired in the graphene laboratory and the FF background follow the same monotonically decreasing trend. In the graphene laboratory, the PNC values are below the significant value for all times except at the beginning of the phase. The feature at about 10:41 a.m. is present in the graphene laboratory and in the background FF and may therefore not be strictly linked to the operations carried out during the phase. At 11:50 a.m. in the graphene laboratory, the PNC decreases from 6892 to 1146 particles per cm^3, with a corresponding increase of the average diameter from 38 to 112 nm. The

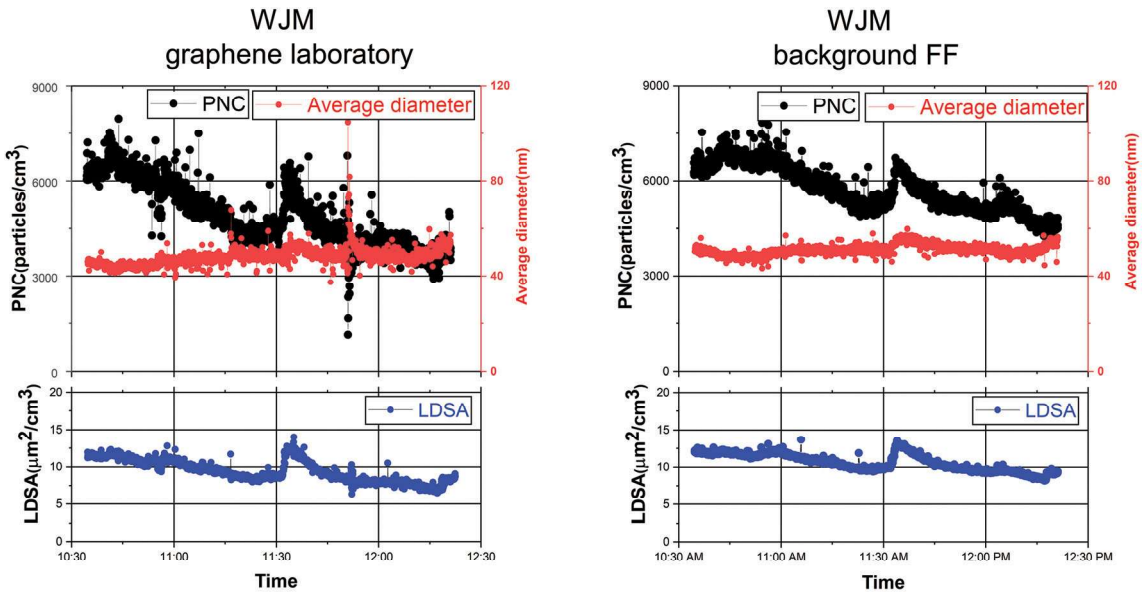

Fig. 3 PNC (black curve), average diameter (red curve) and LDSA concentration (blue curve) during the WJM phase in the graphene laboratory (left side) and the background FF (right side).

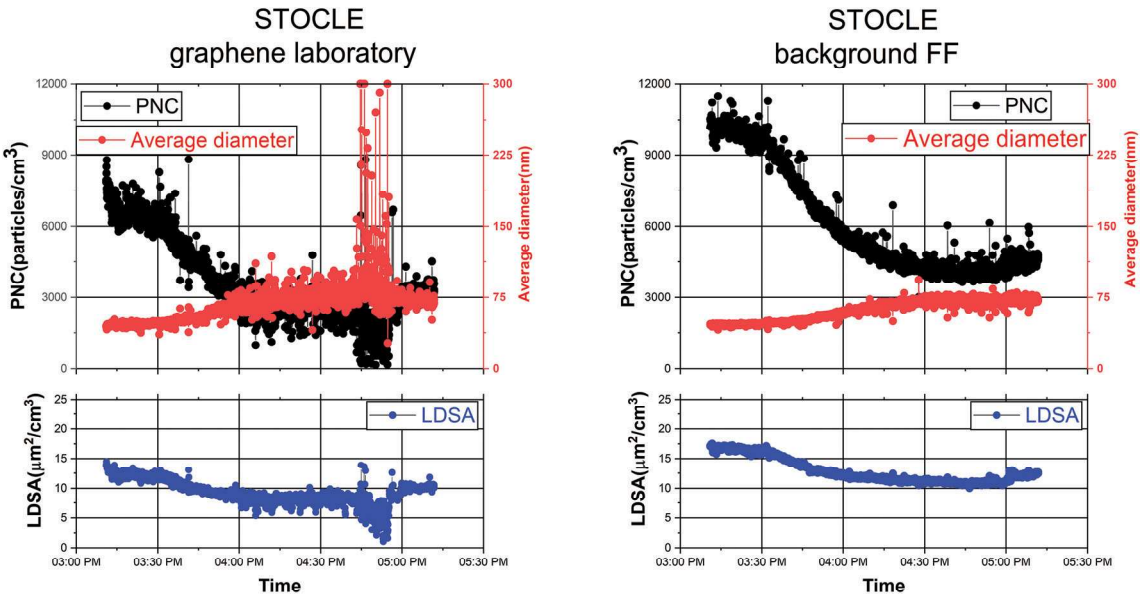

Fig. 4 PNC (black curve), average diameter (red curve) and LDSA concentration (blue curve) during the STOCLE phase in the graphene laboratory (left side) and the background FF (right side).

average particle diameter value during the WJM phase is between 40 to 60 nm. The variations of particle concentration and diameter are probably due to the presence of the volatile organic compounds (VOCS, *i.e.*, NMP, 2-propanol and acetone) used during processing in the WJM phase, as confirmed by the gas chromatography mass spectrometry analysis in Boccuni *et al.*[27] in which the presence of 2.99×10^{-1} ppm of NMP was measured. Molecules of solvent (not only 2-propanol or acetone but also NMP) used in the WJM phase may remain trapped, or "sandwiched", between the aggregated flakes. The condensation of VOCs on the airborne particulates could induce a decrease in the PNC corresponding to an increase of the average diameter.[27,38]

During the STOCLE phase (Fig. 4), the PNC time series follow the same trend. Particularly, in the laboratory the PNC values are lower than those of the FF background, probably due to the ventilation and air extraction conditions.

From 3:11 pm to 4:15 pm, when the freeze dryers were opened to unload the Petri dishes, the PNC values in the laboratory dropped to 29%, from 8797 particles per cm^3 to 2526 particles per cm^3, while the background FF dropped 43%, from 10 513 particles per cm^3 to 4569 particles per cm^3. These important decreases could be related to the RH variation (Fig. 2b) following the forced off ventilation in both the graphene laboratory and in the background FF, highlighting how environmental variables can influence both area and personal measurements, in agreement with previous reports.[27,39] Furthermore, it is qualitatively appreciable that the PNC measured by DM in the graphene laboratory (personal sampling) has a signal to noise ratio larger than that in the FF background due to the fact that during the STOCLE phase, the workers managed and stored the FLG in powder form.

Then, starting at 4:43 pm and lasting about ten minutes, the PNC shows a remarkable feature inside the laboratory, but not in the background FF: a drop which corresponds to an increase of the average diameter up to its maximum recordable value of 300 nm. As in the case of the WJM phase, the worker was using VOCs (2-propanol and acetone) to clean the freeze dryers and hence it is possible that the decrease in the particle number concentration corresponding to an increase of the average diameter could be attributed to the condensation of VOCs on airborne particulate matter in the graphene laboratory.[27,38]

PNC values during the WJM and STOCLE phases were lower than the NRV values for particles with a density lower than 6 g cm^{-3}.[20]

Finally, the LDSA time series obtained by DMs during the WJM (Fig. 3) and STOCLE (Fig. 4) phases both have the same trend as PNC. The mean LDSAs (standard deviation in parenthesis) during WJM are 9.4 (1.5) μm^2 cm^{-3} and 10.6 (1.2) μm^2 cm^{-3}, while during STOCLE they are 9.3 (1.9) μm^2 cm^{-3} and 12.8 (2.1) μm^2 cm^{-3} for the laboratory and background FF, respectively. In any case, the mean values of LDSA inside the graphene laboratory in both phases are much lower than those obtained in different occupational environments.[33,35]

The PNC and LDSA results cannot exclude the release of FLG into the graphene laboratory during the WJM and the STOCLE phases. This measurement strategy allows the characterisation of the particulates collected by filters in the Sioutas inertial impactor through electron microscopy, energy-dispersive X-ray spectroscopy and Raman spectroscopy.

Off-line FLG characterization

Scanning electron microscopy was carried out on all Sioutas filter stages. Particles morphologically similar to those of the

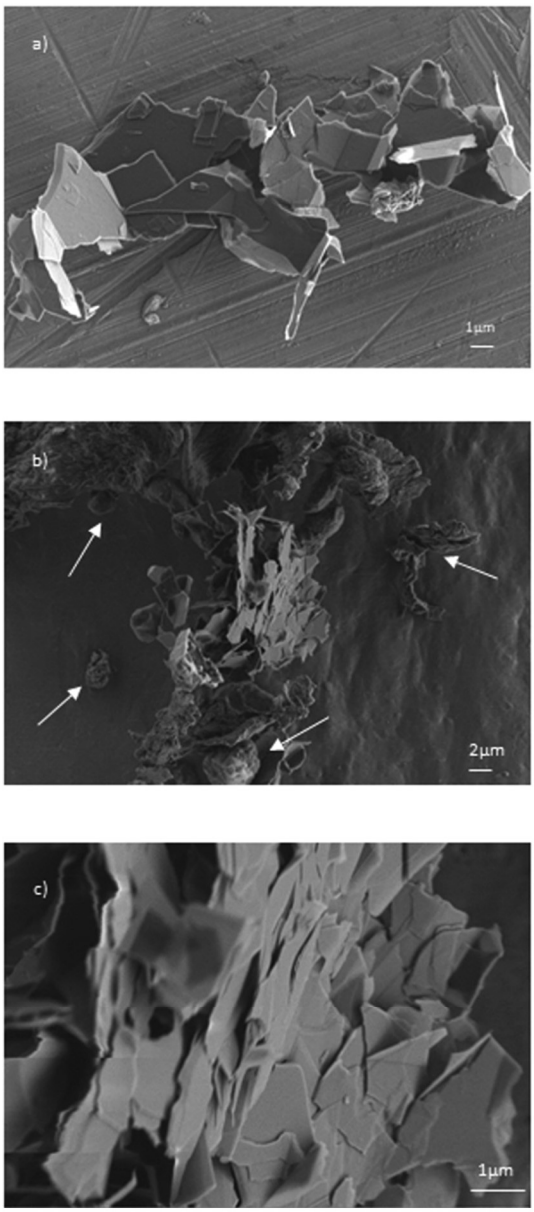

Fig. 5 High resolution SEM images of (a) the trial sample, FLG as obtained at the end of the production phases, and (b and c) flakes collected on the Sioutas filter stage A.

trial sample were found only on filter stage A, in which the coarsest fraction of collected particles has an aerodynamic diameter greater than 2500 nm. The high resolution SEM image of the trial sample (Fig. 5a) shows aggregated flakes. The aggregate of several flakes has lateral dimensions of about 15 μm.

The image obtained of the Sioutas filter stage A (Fig. 5b) shows evidence of aggregated flakes mixed with other airborne particles (see arrows in Fig. 5b) collected during the production phases. EDS analysis on particles similar to those in Fig. 5b (not published) with a size between 1 to 5 μm revealed the presence of C, Na, Si, Mg, Ca and S elements, which are typical elements found in airborne particulate matter.[40] Fig. 5c exhibits a similar morphology (overlapping flakes) and the presence of flakes with different lateral sizes than the trial sample. A raw estimation of aggregate thickness can be deduced considering the unusual aerodynamic properties of graphene.[30] Deposition in the respiratory tract is determined by aerodynamic diameter (d_{ae}), which is defined as the diameter of a sphere of unit density with the same terminal settling velocity as the particle itself.[41] Assuming a platelet-like structure, the aerodynamic diameter (d_{ae}) of FLG can be estimated[42] as

$$d_{ae} = \sqrt{\frac{9\pi\rho t d_{proj}}{16\rho_0}} \quad (1)$$

where t is the platelet thickness, d_{proj} is the projected diameter, ρ_0 is the unit density and ρ is the graphite density (2.26 gr cm^{-3}). The projected diameter (d_{proj} = 8823 nm) was calculated as the equivalent diameter of a particle having the same area of the aggregated flakes shown in Fig. 5c. d_{ae} was calculated, following eqn (1), for the same d_{proj} and for different thickness values (t). In Table 2, it is clear that, for the same d_{proj}, the smaller the thickness, the more the d_{ae} differs from d_{proj}.

In terms of risk assessment, the aerodynamic property of platelet-like particles implies that they could penetrate and deposit in a deeper tract of the respiratory system[43,44] if d_{ae} is lower than d_{proj} as electron microscopy suggests.[42]

Moreover, an indirect estimation of the aggregate thickness greater than 200 nm can be obtained by considering the flakes found on the Sioutas filter stage A, which collects particles with aerodynamic diameters greater than 2500 nm (Table 2).

Either the FLG aggregate or the airborne particles (Fig. 5) may be able to reach the tracheobronchial part of the respiratory system and the particles could be carriers of FLG.[27] Once in the respiratory system, the FLG could be separated from the carriers and reach the deeper sections of the respiratory system.[17]

Raman spectroscopy (Fig. 6), EDS (Fig. 7), TEM analysis and SAED (Fig. 8) were carried out on the Sioutas filter stage A. Raman spectroscopy is a fast and non-destructive technique widely used to identify the number of layers, defects, doping, disorder and chemical modifications of graphene.[45,46] The

Table 2 Projected diameter (d_{proj}) obtained by SEM, thickness values (t) and calculated aerodynamic diameter (d_{ae})

d_{proj} (nm)	t (nm)	d_{ae} (nm)
8823	20	789
	50	1248
	100	1765
	200	2497
	300	3058
	400	3531
	500	3948
	600	4324

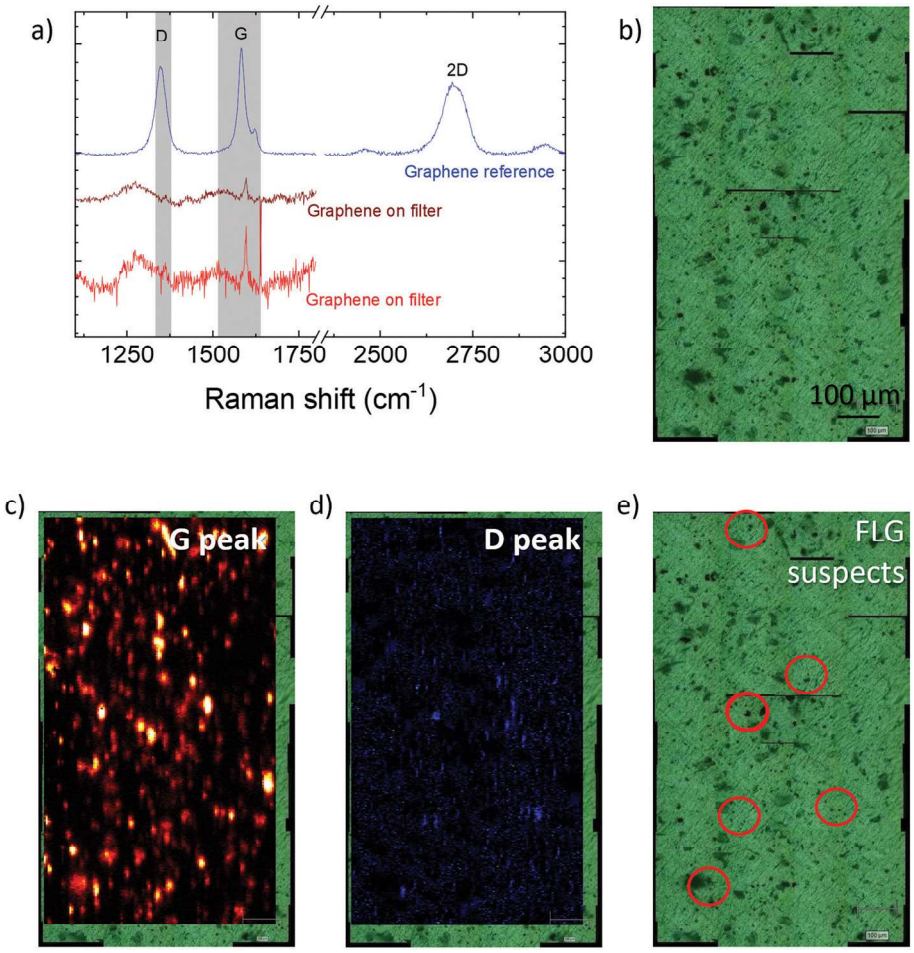

Fig. 6 (a) In blue, Raman spectrum of the FLG powder used as control, showing the D, G and 2D features. In dark and light red are shown the spectra of suspected graphene particles deposited on the filters, the high signal to noise ratio (1 : 10) made the 2D band undetectable. (b) Optical microscope collage of the mapping zone. (c) Raman mapping showing in red tonalities the integral intensity of the G peak, with brightness corresponding to intensity. (d) Raman mapping showing in blue tonalities the integral intensity of the D peak, with brightness corresponding to intensity. (e) The red circles show the zones where the suspected FLG materials with both G and D peak features are found.

Raman spectrum of graphene is composed mainly of the G, D and 2D bands. The G peak corresponds to the E_{2g} phonon at the Brillouin zone centre.[47] The D peak is due to the breathing modes of sp^2 rings and requires a defect for its activation by double resonance.[45,46,48] The 2D peak is the second order of the D peak.[46] This is a single peak in monolayer graphene, whereas it splits in multi-layer graphene, reflecting the evolution of the band structure.[46] The 2D peak is always seen, even when no D peak is present, since no defects are required for the activation of two phonons with the same momentum, one backscattered from the other.[46] Double resonance can also happen as an intra-valley process, *i.e.* connecting two points belonging to the same cone around K or K′.[46] In the Raman spectra of the as-produced FLG flakes, the three features, the D, G and 2D bands, are clearly visible (Fig. 6a). In general, the strongest feature in FLG is the G band;[49] for this reason, the G band is used as a reference when performing Raman mappings on the filter surface. Fig. 6a (the spectrum in blue) shows the Raman spectrum of FLG, indicating the D, G and 2D peaks. To confirm the presence of graphene on the filter, the highest intensity features of the FLG Raman spectrum are recorded, meaning that the presence of the G and D bands is a clear indication that the particle is a graphite-related material. Generally, for highly crystalline graphene flakes, the D band is present when the flakes are smaller than the Raman spot-laser (1 µm).[50,51] In this manner, the presence of D and G bands is a guarantee of finding a graphite- or graphene-related material. Fig. 6a (spectra in red) shows selected spectra from two different points on the filter where the G and D band signals were observed. It is important to highlight that the 2D band was not always detectable; often the signal to noise ratio was larger than the 2D integral intensity signal.

To perform the Raman mappings, large area (*ca.* 700 × 1200 µm^2) scans were performed on the filters. Fig. 6b shows a collage of the area of interest where the Raman mapping was performed. Fig. 6c and d show Raman mappings in different colours, corresponding to the respective integral intensities of the G or D peaks taken on every mapping point. Both features,

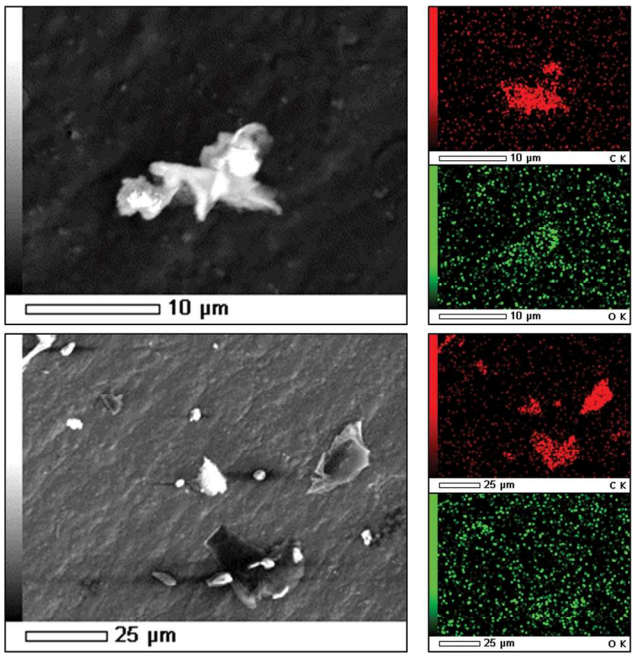

Fig. 7 SEM images and corresponding EDS maps for C (K series) and O (K series) for two flakes collected on the Sioutas filter stage A.

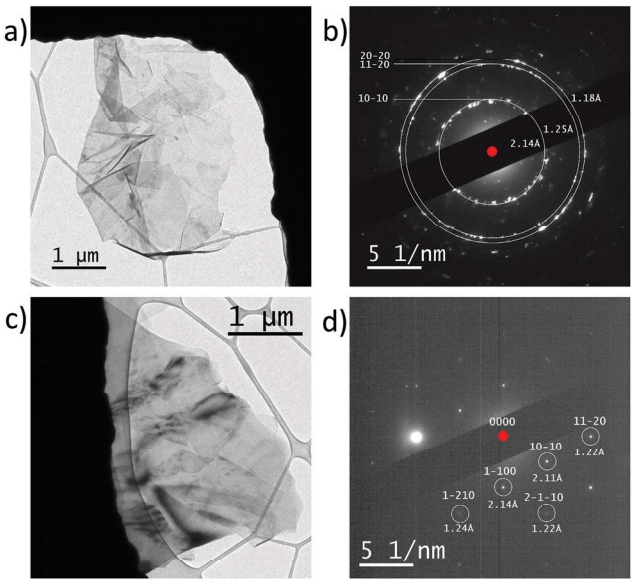

Fig. 8 BF-TEM images of flakes mechanically removed from Sioutas filter stage A (left side) and the corresponding SAED patterns (right side), indexed according to graphite (ICSD 253958).

i.e., the D and the G peaks, were analysed to discard the presence of other impurities or contaminants trapped by the filter that could have Raman signals either in the G or D peak ranges (*ca.* 1350 and 1580 cm^{-1}, respectively). Specifically, the red tonalities in Fig. 6c correspond to the intensity area of the G peak, representing as bright red a spectrum with a clear G band feature; the absence of a G peak feature is represented with black. Similarly, the presence of the D peak in the Raman mapping is represented by a blue tonality in Fig. 6d, in which a light blue colour corresponds to a Raman feature that could indicate a D band. Finally, in Fig. 5e, the zones where the particles displayed both features, a G and a D signal, are circled in red, indicating the high probability of finding a graphene- or graphite-related material.

To verify the presence of graphene-like materials, SEM was performed on the red-encircled areas identified by the Raman mappings. Fig. 7 shows SEM images with the corresponding EDS maps of C and O, showing that both suspected materials are mainly formed by carbon atoms with few oxygen atoms. It is worth stressing that the results obtained by Raman spectroscopy integrated with SEM microscopy show that the material collected on the Sioutas filter A is highly likely to be FLG that was produced in the graphene laboratory. The advantage of using these techniques lies in the fact that they are non-destructive characterization techniques in which the sampled filter is not subjected to post collection treatments, thus allowing the highlighting of some important characteristics of the airborne nanomaterial, such as the aggregation state.

After mapping the graphene features over the Sioutas filter stage A *via* Raman spectroscopy, SEM imaging and SEM-EDS compositional mapping, TEM and SAED analysis were needed to confirm the crystal structure of graphene within the flake-shaped objects in the region of interest on Sioutas filter A. Due to the fact that the Sioutas filter A is not electron-transparent, preparation of the sample for TEM required a destructive procedure (see Materials and methods section) on the identified area of interest. TEM and SAED analysis took place after the SEM and Raman investigations to evidence the unique characteristics of the crystal structure of FLG.

The Sioutas filter stage A was characterized by TEM and SAED. Both BF-TEM images (Fig. 8a and c) show flakes lying flat on the support film, with a slightly wrinkled surface. The SAED pattern in Fig. 8d can be indexed as a single-crystal [0001]-oriented graphite pattern (using the Miller-Bravais indices), as in typical FLG produced by liquid phase exfoliation,[52] whereas the polycrystalline-like ring pattern in the diffraction pattern in Fig. 8b highlighted a pattern ascribable to superimposed flakes, stacked, each of them with a preferential [0001]-orientation. TEM analysis analyses confirmed that the Sioutas filter A collected rare FLG dispersed in the graphene laboratory during the monitored production phases.

Conclusions

In the present work, the assessment of exposure to airborne FLG was carried out in the research laboratory where FLG is produced by the freeze-drying of graphene ink obtained by the LPE of graphite layered crystals.

On the basis of OECD methodology, high resolution real time measurements and time-integrated samplings were per-

formed in the workplace during the WJM and the STOCLE production phases. In the graphene laboratory, microclimatic variables were also measured to consider the overall exposure scenario. Moreover, off-line analysis through electron microscopies and Raman spectroscopy were carried out to characterize the airborne particles collected in the workers' PBZ by the Sioutas inertial impactor.

The major findings of the present study are summarized as follows:

PNC values in the graphene laboratory were influenced by environmental conditions (*i.e.*, the forced ventilation system) during the following production phases.

The PNC, average diameter and LDSA values acquired from the worker's PBZ, compared to those obtained simultaneously in the background FF, did not exclude the potential release of FLG, in particular during the cleaning operations and storing activity in which FLG was in powder form.

HR-SEM analysis on the Sioutas filters highlights the presence of particles having a similar morphology with the FLG trial sample. In addition, the projected diameter of plate-like particles was obtained from the SEM image. In terms of risk assessment, the aerodynamic property of platelet-like particles implies that they could penetrate and deposit in a deeper section of the respiratory system considering an aerodynamic diameter lower than the projected diameter, as electron microscopy suggests.

An indirect method was proposed to roughly estimate the FLG thickness (greater than 200 nm) by integrating information obtained by SEM image and the aerodynamic properties of the FLG collected on the Sioutas filter.

Raman spectra recorded on the Sioutas filter stage showed obvious G and D band features, a clear indication that the particle is a graphite-related material.

SEM and EDS signals on specific areas identified by Raman mapping confirm that the material is mainly formed of carbon atoms with a small amount of oxygen atoms. The results obtained by Raman spectroscopy integrated with SEM microscopy show that the material collected on the Sioutas filter is highly likely to be FLG produced in the graphene laboratory.

TEM showed flakes lying flat on the support film and the SAED patterns can be attributed to single-crystal [0001]-oriented graphite flakes, in some cases stacked on each other.

The results confirm the need to improve risk management strategies already in force in the graphene laboratory during FLG production process, such as regular maintenance programs and effective collective (*e.g.* aspiration hoods) and personal (*e.g.* gloves, glasses, masks and safety clothing) protective equipment. The risk management hierarchy should primarily include the possibility to contain those phases with higher risk through the implementation of closed systems, glove boxes or ventilated boxes.[27,53] Furthermore, it is possible to organize the processes by implementing specific procedures and shifts with a view to reducing working times. Lastly, personal protective equipment should be worn by workers inside the laboratory during all phases in which contact with the material in powder form may occur.

Finally, the integration of real time measurements with microscopy and spectroscopy characterizations allowed the identification and characterization of the airborne FLG morphology, elemental composition and lattice parameter structure.

The information so-obtained provides a valuable basis for improving risk management strategies in R&D, as already recommended in Boccuni *et al.*,[27] and demonstrates the importance of integrating multiple characterization methods in order to analyse complex exposure scenarios such as graphene production workplaces.

Author contributions

Conceptualization: Francesca Tombolini, Fabio Boccuni, Riccardo Ferrante, Stefania Sabella and Sergio Iavicoli. Data curation: Francesca Tombolini, Fabio Boccuni, Riccardo Ferrante, Claudio Natale, Esau Del Rio Castillo, Luca Leoncino. Formal analysis: Francesca Tombolini, Fabio Boccuni, Riccardo Ferrante, Claudio Natale, Esau Del Rio Castillo, Luca Leoncino. Investigation: Francesca Tombolini, Fabio Boccuni, Riccardo Ferrante, Luigi Marasco, Elisa Mantero. Methodology: Francesca Tombolini, Fabio Boccuni, Riccardo Ferrante. Resources: Vittorio Pellegrini, Sergio Iavicoli. Supervision: Fabio Boccuni, Vittorio Pellegrini, Stefania Sabella, Sergio Iavicoli. Visualization: Francesca Tombolini, Esau Del Rio Castillo, Luca Leoncino. Writing-original draft: Francesca Tombolini, Fabio Boccuni, Riccardo Ferrante, Esau Del Rio Castillo, Luca Leoncino. Writi ng-review & editing: Francesca Tombolini, Fabio Boccuni, Riccardo Ferrante, Claudio Natale, Esau Del Rio Castillo, Luca Leoncino, Vittorio Pellegrini, Stefania Sabella, Sergio Iavicoli.

Conflicts of interest

There are no conflicts to declare.

Acknowledgements

The present study is part of the Project "Nano and Key enabling technologies within the innovation processes: risk and opportunities in occupational settings by prevention through design (NanoKey)", funded by the Italian Workers' Compensation Authority (INAIL) and coordinated in cooperation between the INAIL Department of Occupational and Environmental Medicine Epidemiology and Hygiene, and the Italian Institute of Technology (IIT). The findings and conclusions in this publication are those of the authors and do not necessarily represent the views of the employing organizations.

We are grateful to Dr Rosaria Brescia from Italian Institute of Technology, Italy, for her expert collaboration about TEM and SAED characterization technique.

References

1 J. Jeevanandam, A. Barhoum, Y. S. Chan, A. Dufresne and M. K. Danquah, *Beilstein J. Nanotechnol.*, 2018, **9**, 1050–1074.

2 Y. S. Lee, J. H. Sung, K. S. Song, J. K. Kim, B. S. Choi, I. J. Yu and J. D. Park, *Toxicol. Res.*, 2019, **8**, 580–586.

3 K. Novoselov, A. Geim, S. Morozov, D. Jiang, Y. Zhang, S. Dubonos, I. Grigorieva and A. Firsov, *Science*, 2004, **306**, 666–669.

4 A. C. Ferrari, F. Bonaccorso, V. Fal'ko, K. S. Novoselov, S. Roche, P. Bøggild, S. Borini, F. H. L. Koppens, V. Palermo, N. Pugno, J. A. Garrido, R. Sordan, A. Bianco, L. Ballerini, M. Prato, E. Lidorikis, J. Kivioja, C. Marinelli, T. Ryhänen, A. Morpurgo, J. N. Coleman, V. Nicolosi, L. Colombo, A. Fert, M. Garcia-Hernandez, A. Bachtold, G. F. Schneider, F. Guinea, C. Dekker, M. Barbone, Z. Sun, C. Galiotis, A. N. Grigorenko, G. Konstantatos, A. Kis, M. Katsnelson, L. Vandersypen, A. Loiseau, V. Morandi, D. Neumaier, E. Treossi, V. Pellegrini, M. Polini, A. Tredicucci, G. M. Williams, B. Hee Hong, J. H. Ahn, J. Min Kim, H. Zirath, B. J. Van Wees, H. Van Der Zant, L. Occhipinti, A. Di Matteo, I. A. Kinloch, T. Seyller, E. Quesnel, X. Feng, K. Teo, N. Rupesinghe, P. Hakonen, S. R. T. Neil, Q. Tannock, T. Löfwander and J. Kinaret, *Nanoscale*, 2015, **7**, 4598–4810.

5 P. Avouris and C. Dimitrakopoulos, *Mater. Today*, 2012, **15**, 86–97.

6 A. E. Del Rio Castillo, V. Pellegrini, A. Ansaldo, F. Ricciardella, H. Sun, L. Marasco, J. Buha, Z. Dang, L. Gagliani, E. Lago, N. Curreli, S. Gentiluomo, F. Palazon, M. Prato, R. Oropesa-Nuñez, P. S. Toth, E. Mantero, M. Crugliano, A. Gamucci, A. Tomadin, M. Polini and F. Bonaccorso, *Mater. Horiz.*, 2018, **5**, 890–904.

7 R. Hawaldar, P. Merino, M. R. Correia, I. Bdikin, J. Grácio, J. Méndez, J. A. Martín-Gago and M. K. Singh, *Sci. Rep.*, 2012, **2**, 2–10.

8 J. H. Lee, J. H. Han, J. H. Kim, B. Kim, D. Bello, J. K. Kim, G. H. Lee, E. K. Sohn, K. Lee, K. Ahn, E. M. Faustman and I. J. Yu, *Inhalation Toxicol.*, 2016, **28**, 281–291.

9 L. Chen, Y. Hernandez, X. Feng and K. Müllen, *Angew. Chem., Int. Ed.*, 2012, **51**, 7640–7654.

10 J. Peng, W. Gao, B. K. Gupta, Z. Liu, R. Romero-Aburto, L. Ge, L. Song, L. B. Alemany, X. Zhan, G. Gao, S. A. Vithayathil, B. A. Kaipparettu, A. A. Marti, T. Hayashi, J. J. Zhu and P. M. Ajayan, *Nano Lett.*, 2012, **12**, 844–849.

11 D. Guarnieri, P. Sánchez-Moreno, A. E. Del Rio Castillo, F. Bonaccorso, F. Gatto, G. Bardi, C. Martín, E. Vázquez, T. Catelani, S. Sabella and P. P. Pompa, *Small*, 2018, **14**, 1–11.

12 B. Zhang, Y. Wang and G. Zhai, *Mater. Sci. Eng., C*, 2016, **61**, 953–964.

13 X. Gao and G. V. Lowry, *NanoImpact*, 2018, **9**, 14–30.

14 M. Pelin, S. Sosa, M. Prato and A. Tubaro, *Nanoscale*, 2018, **10**, 15894–15903.

15 P. A. Schulte, C. L. Geraci, V. Murashov, E. D. Kuempel, R. D. Zumwalde, V. Castranova, M. D. Hoover, L. Hodson and K. F. Martinez, *J. Nanopart. Res.*, 2014, **16**, 2153–2170.

16 W. Heitbrink, L.-M. Lo and K. Dunn, *J. Occup. Environ. Hyg.*, 2015, **12**, 16–28.

17 B. Fadeel, C. Bussy, S. Merino, E. Vázquez, E. Flahaut, F. Mouchet, L. Evariste, L. Gauthier, A. J. Koivisto, U. Vogel, C. Martín, L. G. Delogu, T. Buerki-Thurnherr, P. Wick, D. Beloin-Saint-Pierre, R. Hischier, M. Pelin, F. Candotto Carniel, M. Tretiach, F. Cesca, F. Benfenati, D. Scaini, L. Ballerini, K. Kostarelos, M. Prato and A. Bianco, *ACS Nano*, 2018, **12**, 10582–10620.

18 D. Cavallo, A. Ciervo, A. M. Fresegna, R. Maiello, P. Tassone, G. Buresti, S. Casciardi, S. Iavicoli and C. L. Ursini, *J. Appl. Toxicol.*, 2015, **35**, 1102–1113.

19 A. Spinazzè, A. Cattaneo, F. Borghi, L. Del Buono, D. Campagnolo, S. Rovelli and D. M. Cavallo, *Int. J. Hyg. Environ. Health*, 2019, **222**, 76–83.

20 P. Oberbek, P. Kozikowski, K. Czarnecka, P. Sobiech, S. Jakubiak and T. Jankowski, *J. Nanopart. Res.*, 2019, **21**, 222–246.

21 R. Mihalache, J. Verbeek, H. Graczyk, V. Murashov and P. van Broekhuize, *Nanotoxicology*, 2017, **11**, 7–19.

22 H. S. Lee, B. Balasubramanian, G. V. T. Gopalakrishna, S. J. Kwon, S. P. Karthick and V. Saraswathy, *Constr. Build. Mater.*, 2018, **159**, 463–472.

23 D. M. Brown, M. R. Wilson, W. MacNee, V. Stone and K. Donaldson, *Toxicol. Appl. Pharmacol.*, 2001, **175**, 191–199.

24 H. Kuuluvainen, T. Rönkkö, A. Järvinen, S. Saari, P. Karjalainen, T. Lähde, L. Pirjola, J. V. Niemi, R. Hillamo and J. Keskinen, *Atmos. Environ.*, 2016, **136**, 105–113.

25 Organization for Economic Cooperation and Development (OECD), *ENV/JM/MONO*, 2015, **19**, Available online: http://www.oecd.org/officialdocuments/publicdisplaydocumentpdf/?cote=env/jm/mono(2010)47&doclanguage=en (accessed December 23, 2020).

26 Organization for Economic Cooperation and Development (OECD), *ENV/JM/MONO*, 2017, **30**, Available online: http://www.oecd.org/officialdocuments/publicdisplaydocumentpdf/?cote=env/jm/mono(2015)19&doclanguage=en (accessed on 23 December, 2020).

27 F. Boccuni, R. Ferrante, F. Tombolini, C. Natale, A. Gordiani, S. Sabella and S. Iavicoli, *Nanotoxicology*, 2020, **14**, 1280–1300.

28 C. L. Ursini, A. M. Fresegna, A. Ciervo, R. Maiello, V. Del Frate, D. Poli, G. Folesani, G. Buresti, L. Di cristo, S. Sabella, M. A. Malvindi, S. Iavicoli and D. Cavallo, *Nanotoxicology*, 2020, 1–15.

29 S. Bellani, F. Wang, G. Longoni, L. Najafi, R. Oropesa-nuñez, A. E. Del, R. Castillo, M. Prato, X. Zhuang and V. Pellegrini, *Nano Lett.*, 2018, **18**, 7155–7164.

30 A. E. Del Río Castillo and F. Bonaccorso, *Carbon*, submitted.

31 R. Ferrante, F. Boccuni, F. Tombolini and S. Iavicoli, in *Nanotechnology in Eco-efficient Construction*, ed. S. A. F. Pacheco-Torgal, M. V. Diamanti, A. Nazari, C. G. Granqvist and A. Pruna, 2018, pp. 785–813.

32 C. Asbach, H. Kaminski, D. Von Barany, T. A. J. Kuhlbusch, C. Monz, N. Dziurowitz, J. Pelzer, K. Vossen, K. Berlin, S. Dietrich, U. Götz, H. J. Kiesling, R. Schierl and D. Dahmann, *Ann. Occup. Hyg.*, 2012, **56**, 606–621.

33 I. Bellagamba, F. Boccuni, R. Ferrante, F. Tombolini, F. Marra, M. S. Sarto and S. Iavicoli, *Nanomaterials*, 2020, **10**, 1520.

34 D. Brouwer, B. V. D. Markus, M. Berges, E. Jankowska, D. Bard and D. Mark, *J. Nanopart. Res.*, 2009, **11**, 1687–1881.

35 O. Geiss, I. Bianchi and J. Barrero-Moreno, *J. Aerosol Sci.*, 2016, **96**, 24–37.

36 Internatiional Commission on Radiological Protection (ICRP), *Ann. ICRP*, 1994, **24**, 1–482.

37 A. S. Fonseca, A. Maragkidou, M. Viana, X. Querol, K. Hämeri, I. de Francisco, C. Estepa, C. Borrell, V. Lennikov and G. F. de la Fuente, *Sci. Total Environ.*, 2015, **565**, 922–932.

38 E. G. Schnitzler, A. Dutt, A. M. Charbonneau, J. S. Olfert and W. Jäger, *Environ. Sci. Technol.*, 2014, **48**, 14309–14316.

39 F. Boccuni, R. Ferrante, F. Tombolini, D. Lega, A. Antonini, A. Alvino, P. Pingue, F. Beltram, L. Sorba, V. Piazza, M. Gemmi, A. Porcari and S. Iavicoli, *Int. J. Mol. Sci.*, 2018, **19**, 349–378.

40 A. D'Alessandro, F. Lucarelli, P. A. Mandò, G. Marcazzan, S. Nava, P. Prati, G. Valli, R. Vecchi and A. Zucchiatti, *J. Aerosol Sci.*, 2003, **34**, 243–259.

41 W. Hinds, *Aerosol Technology_ Properties, Behavior, and Measurement of Airborne Particles*, 1999.

42 A. Schinwald, F. A. Murphy, A. Jones, W. MacNee and K. Donaldson, *ACS Nano*, 2011, **6**, 736–746.

43 W. Netkueakul, D. Korejwo, T. Hammer, S. Chortarea, P. Rupper, O. Braun, M. Calame, B. Rothen-Rutishauser, T. Buerki-Thurnherr, P. Wick and J. Wang, *Nanoscale*, 2020, **12**, 10703–10722.

44 W. C. Su, B. K. Ku, P. Kulkarni and Y. S. Cheng, *J. Occup. Environ. Hyg.*, 2016, **13**, 48–59.

45 A. C. Ferrari and J. Robertson, *Phys. Rev. B: Condens. Matter Mater. Phys.*, 2001, **64**, 075414.

46 A. C. Ferrari, J. C. Meyer, V. Scardaci, C. Casiraghi, M. Lazzeri, F. Mauri, S. Piscanec, D. Jiang, K. S. Novoselov, S. Roth and A. K. Geim, *Phys. Rev. Lett.*, 2006, **97**, 1–4.

47 A. C. Ferrari and D. M. Basko, *Nat. Nanotechnol.*, 2013, **8**, 235–246.

48 A. C. Ferrari and J. Robertson, *Phys. Rev. B: Condens. Matter Mater. Phys.*, 2000, **61**, 14095.

49 L. M. Malard, M. A. Pimenta and G. Dresslhaus, *Phys. Rep.*, 2009, **473**, 51–87.

50 R. Beams, L. G. Cancado and L. Novotny, *J. Phys.: Condens. Matter*, 2015, **27**, 083002.

51 A. Das, B. Chakraborty and A. K. Sood, *Bull. Mater. Sci.*, 2008, **31**, 579–584.

52 H. Sun, A. E. Del Rio Castillo, S. Monaco, A. Capasso, A. Ansaldo, M. Prato, D. A. Dinh, V. Pellegrini, B. Scrosati, L. Manna and F. Bonaccorso, *J. Mater. Chem. A*, 2016, **4**, 6886–6895.

53 F. Boccuni, B. Rondinone, C. Petyx and S. Iavicoli, *J. Cleaner Prod.*, 2007, **16**, 949–956.